

Efficient Adaptation of Pre-trained Vision Transformer underpinned by Approximately Orthogonal Fine-Tuning Strategy

Yiting Yang¹, Hao Luo¹, Yuan Sun², Qingsen Yan³, Haokui Zhang³, Wei Dong^{1*},
Guoqing Wang², Peng Wang², Yang Yang², Hengtao Shen⁴

¹ Xi'an University of Architecture and Technology

² University of Electronic Science and Technology of China

³ Northwestern Polytechnical University ⁴ TongJi University

Abstract

A prevalent approach in Parameter-Efficient Fine-Tuning (PEFT) of pre-trained Vision Transformers (ViT) involves freezing the majority of the backbone parameters and solely learning low-rank adaptation weight matrices to accommodate downstream tasks. These low-rank matrices are commonly derived through the multiplication structure of down-projection and up-projection matrices, exemplified by methods such as LoRA and Adapter. In this work, we observe an approximate orthogonality among any two row or column vectors within any weight matrix of the backbone parameters; however, this property is absent in the vectors of the down/up-projection matrices. Approximate orthogonality implies a reduction in the upper bound of the model's generalization error, signifying that the model possesses enhanced generalization capability. If the fine-tuned down/up-projection matrices were to exhibit this same property as the pre-trained backbone matrices, could the generalization capability of fine-tuned ViTs be further augmented? To address this question, we propose an Approximately Orthogonal Fine-Tuning (AOFT) strategy for representing the low-rank weight matrices. This strategy employs a single learnable vector to generate a set of approximately orthogonal vectors, which form the down/up-projection matrices, thereby aligning the properties of these matrices with those of the backbone. Extensive experimental results demonstrate that our method achieves competitive performance across a range of downstream image classification tasks, confirming the efficacy of the enhanced generalization capability embedded in the down/up-projection matrices. Our code is available at link¹.

1. Introduction

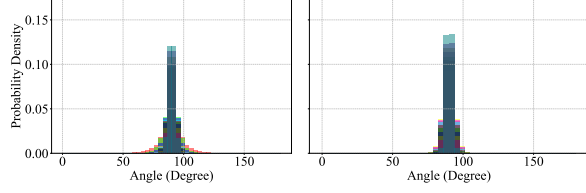
To leverage the strengths of pre-trained Vision Transformers (ViT) [4] for specific downstream applications, Parameter-Efficient Fine-Tuning (PEFT) strategy has gained significant attention. This PEFT [1, 9–11, 14] strategy aims to minimize the number of parameters that need to be updated, thereby enhancing computational efficiency and reducing storage requirements. A prevalent approach within PEFT involves freezing the majority of the backbone parameters of the ViT and focusing on learning low-rank adaptation weight matrices to accommodate the nuances of different downstream tasks. Methods such as LoRA [10] (Low-Rank Adaptation) and Adapter [9] have exemplified this approach by deriving low-rank matrices through the multiplication structure of down- and up-projection matrices. These matrices act as intermediary layers that facilitate the adaptation of the frozen backbone to new tasks, while keeping the number of learnable parameters to a minimum.

Upon closer examination of the backbone parameters of ViTs, an interesting observation emerges: the weight matrices within the backbone parameters after pre-training exhibit an approximate orthogonality among any two row or column vectors, as shown in Fig. 1. Orthogonality is a fundamental property in linear algebra that signifies the independence of vectors within a matrix. When any two vectors in the weight matrix are approximately orthogonal, it subtly suggests that the model has a smaller upper bound on generalization error and thus possesses an enhanced generalization capability. The detailed analysis of the upper bound on generalization error is shown in Section 3.3.

However, this desirable orthogonal property is notably absent in the vectors of the down/up-projection matrices used in current PEFT [9, 10] methods, as shown in Fig. 2. This discrepancy raises an intriguing question: if the down/up-projection matrices were to exhibit the same approximate orthogonality as the backbone matrices, could the generalization capability of fine-tuned ViTs be further

*Corresponding author. (dongwei156@xauat.edu.cn)

¹https://drive.google.com/file/d/1rg3JYfkmelGDbRWXspO22wxVspbtntHv/view?usp=drive_link



(a) The angle distribution of pre-trained matrices \mathbf{W}_q . (b) The angle distribution of pre-trained matrices \mathbf{W}_v .

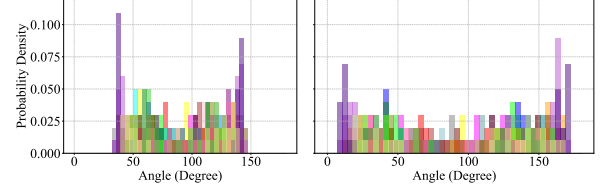
Figure 1. Illustration of approximate orthogonality among any two column vectors of weight matrices $\mathbf{W}_q, \mathbf{W}_v$, in the ViT-B model. The histogram represents the distribution of angles between any two column vectors within each weight matrix. Specifically, (a) and (b) represent approximate orthogonality in the pre-trained model. The whole results and their legends can be found in Appendix A.

augmented? In other words, could aligning the properties of these adaptation matrices with those of the backbone lead to improved performance in downstream tasks?

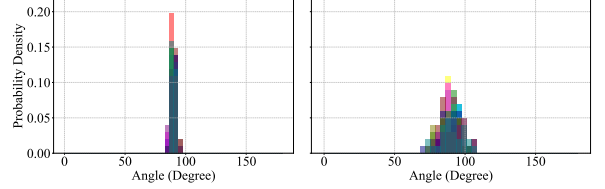
To explore this hypothesis, we propose a novel Approximately Orthogonal Fine-Tuning (AOFT) strategy for representing the low-rank weight matrices in PEFT. Our approach aims to align the properties of the down/up-projection matrices with those of the backbone matrices by enforcing approximate orthogonality. Specifically, we employ a single learnable vector to generate a set of approximately orthogonal vectors, which are then used to construct the down/up-projection matrices. The rationale behind this strategy is grounded in the theoretical understanding of orthogonal matrices. Orthogonal matrices are known for their numerical stability, efficient computation, and ability to preserve the norm of vectors [8, 28]. When approximate orthogonal weight matrices are used to replace the down/up-projection matrices, the upper bound of the model’s generalization error decreases, thereby enhancing the model’s generalization capability.

To validate the efficacy of our AOFT strategy, we conducted extensive experiments across a range of downstream image classification tasks. Our results demonstrate that the proposed method achieves competitive performance compared to existing PEFT techniques. These findings not only confirm the hypothesis that enforcing orthogonality in the down/up-projection matrices can augment the generalization capability of fine-tuned ViTs but also highlight the potential of our AOFT strategy as a powerful tool for PEFT in computer vision. In summary, the contributions of this work can be summarized as follows:

- We introduce a novel AOFT strategy for aligning the properties of the down/up-projection matrices with those of the backbone matrices by enforcing approximate orthogonality, leveraging the theoretical understanding of orthogonal matrices and their beneficial properties for model representation.
- We utilized a learnable vector to generate down/up-projection matrices with approximately orthogonal



(a) The angle distribution of any two column vectors of down-projection matrix in LoRA. (b) The angle distribution of any two column vectors of up-projection matrix in LoRA.



(c) The angle distribution of any two column vectors of down-projection matrix in Adapter. (d) The angle distribution of any two column vectors of up-projection matrix in Adapter.

Figure 2. The angle distribution between any two column vectors within the down/up-projection matrices in the LoRA and Adapter structures, where (a) and (b) represent the results trained using LoRA method, (c) and (d) represent the results trained using Adapter method. These results are all obtained from models trained on the dtd dataset. Their legends can be found in Appendix A.

row/column vectors, thereby reducing the number of learnable parameters and consequently decreasing the overhead of fine-tuning the model.

- Through extensive experiments across a range of downstream image classification tasks, we demonstrates that the proposed AOFT strategy achieves competitive performance compared to existing PEFT techniques.

2. Related Work

2.1. Parameter-Efficient Fine-Tuning

In contrast to the full fine-tuning technique, which involves learning all parameters, parameter-efficient fine-tuning modifies only a small subset of parameters while keeping the majority of parameters in the model’s backbone frozen. This methodology enables the model to efficiently adapt to downstream tasks, while concurrently achieving substantial reductions in training costs. In the field of PEFT methods, numerous works continue to emerge, constantly driving technological innovation and development [14]. Among them, Adapter method [9], as one of the mainstream techniques for fine-tuning large models, introduces an innovative fine-tuning paradigm by inserting trainable adapter components into the network structure to achieve efficient model adjustment. The Low-Rank Adaptation (LoRA) [10] method designs the adapter as a side path and cleverly utilizes a bottleneck structure to significantly reduce the number of learnable parameters during fine-tuning. This design not only alleviates the computa-

tional burden on the model but also simulates incremental changes in the parameter matrix. Visual Prompt Tuning (VPT) [11] adds a small number of prompt parameters to the input layer and intermediate layers of ViT, and only trains these prompt parameters while keeping the backbone frozen. Adapter Re-Composing (ARC) [2] employs a unique approach using symmetric up-and-down projections to create cross-layer shared bottleneck operations. By learning low-dimensional rescaling coefficients, it effectively reconfigures layer-adaptive adapters, thereby reducing the cost of fine-tuning. Residual-based Low-Rank Rescaling (RLRR) [3] analyzes PEFT methods from the perspective of Singular Value Decomposition (SVD), ensuring through a residual design that new parameters do not deviate excessively from the pre-trained model.

These methods do not introduce approximate orthogonality into their weight matrices to preserve the model’s generalization capability.

2.2. PEFT via Orthogonality

Orthogonal matrices have certain applications in fine-tuning strategies. Orthogonal Fine-Tuning (OFT) [24] preserves the pretrained semantics and concepts by mapping the linear weights with an angle-preserving transformation using a block-diagonal matrix, while adapting to downstream tasks. Quasi-Givens Orthogonal Fine-Tuning (qGOFT) [21] adjusts the pre-trained weight matrix to accommodate different types of downstream tasks by left-multiplying it with a Givens Rotation matrix. Orthogonal Butterfly (BOFT) [17] parameterizes dense orthogonal matrices using the product of multiple sparse orthogonal matrices based on butterfly decomposition.

Our method generates an entire approximately orthogonal down/up-projection matrices through a single vector. This approach is simple and efficient, discarding the fine-tuning of down/up-projection matrices using approximately orthogonal matrices employed by existing methods, thereby enhancing the model’s generalization capability while improving efficiency.

3. Methodology

In this section, we first outline the concepts related to the PEFT methods. Then, we propose a method to replace projection matrices in LoRA and Adapter methods with down/up-projection matrices in which column/row vectors are approximately orthogonal; all these column/row vectors are generated by one vector. Finally, we analyze the effectiveness of approximately orthogonal projection matrices in preserving the model’s generalization capability.

3.1. Preliminary Knowledge

Vision Transformer (ViT) [4] is a deep learning model that applies the Transformer architecture to computer vi-

sion tasks such as image classification. ViT consists of two main components: the Patch Embedding layer and the Transformer Encoder layer. The Patch Embedding layer splits an input image $\mathbf{X} \in \mathbb{R}^{H \times W \times C}$ into fixed-size patches and projects each patch into a sequence; the Transformer Encoder processes the patch embeddings using Multi-Head Attention (MHA) and Feed-Forward Network (FFN) blocks. The computation of the (l) -th Transformer Encoder layer is defined as:

$$\begin{aligned}\mathbf{X}^{(l)'} &= \text{MHA}(\text{LN}(\mathbf{X}^{(l-1)})) + \mathbf{X}^{(l-1)}, \\ \mathbf{X}^{(l)} &= \text{FFN}(\text{LN}(\mathbf{X}^{(l)})) + \mathbf{X}^{(l)},\end{aligned}\quad (1)$$

where $\text{LN}(\cdot)$ is a function to layer representation normalization. In the MHA block, the computation of each attention head is defined as:

$$\begin{aligned}\text{AttentionHead}(\mathbf{X}^{(l-1)}) &= \\ \text{Softmax} \left(\frac{(\mathbf{X}^{(l-1)} \mathbf{W}_q^{(l)})(\mathbf{X}^{(l-1)} \mathbf{W}_k^{(l)})^\top}{\sqrt{D_{\text{head}}^{(l)}}} \right) &\mathbf{X}^{(l-1)} \mathbf{W}_v^{(l)},\end{aligned}\quad (2)$$

where $\mathbf{W}_q^{(l)}, \mathbf{W}_k^{(l)}, \mathbf{W}_v^{(l)} \in \mathbb{R}^{D^{(l-1)} \times D_{\text{head}}^{(l)}}$ are the query, key, and value weight matrices, respectively, $D_{\text{head}}^{(l)}$ is the output dimension of each attention head. MHA is the weighted sum of multiple attention heads according to the weights $\mathbf{W}_o^{(l)}$.

The output of the MHA block is normalized and fed into the FFN block:

$$\text{FFN}(\mathbf{X}^{(l)}) = \text{GELU}(\mathbf{X}^{(l)} \mathbf{W}_{\text{FC1}}^{(l)}) \mathbf{W}_{\text{FC2}}^{(l)}, \quad (3)$$

where $\mathbf{W}_{\text{FC1}}^{(l)} \in \mathbb{R}^{D^{(l)} \times 4 \cdot D^{(l)}}$ and $\mathbf{W}_{\text{FC2}}^{(l)} \in \mathbb{R}^{4 \cdot D^{(l)} \times D^{(l)}}$ are two linear projection matrices.

3.2. Approximately Orthogonal Fine-Tuning

In [22] a method to construct the orthogonal matrix is proposed, and the detailed construction method is provided in Appendix D. Following this construction, we use a learnable vector $\vec{q} = (q_0, q_1, \dots, q_N)^\top \in \mathbb{R}^N$ to generate an orthogonal matrix $\mathbf{Q} \in \mathbb{R}^{N \times N}$, then, we replace down- or up-projection matrix with the orthogonal matrix \mathbf{Q} . This generation operator is defined as:

$$\text{AO}(\vec{q}) = \mathbf{Q}[:, 0 : d], \quad (4)$$

where the d is the dimension of the bottleneck in low-rank adaptation and $[:, :]$ represents indexes for the matrix, used to obtain a submatrix from that matrix. The orthogonal ma-

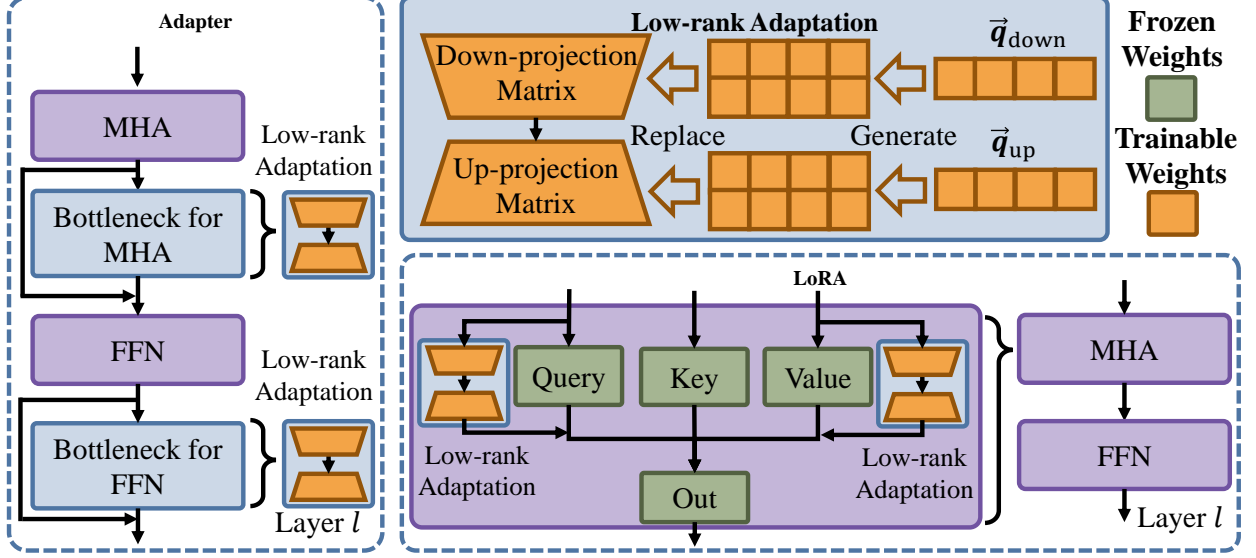


Figure 3. Illustration of the proposed AOFT method: We construct an approximately orthogonal matrix using a learnable vector to replace the up-projection and down-projection matrices in the bottleneck structure. To validate its effectiveness, we apply it to the LoRA and Adapter architectures. (1) Within the Adapter architecture, which itself incorporates a Low-Rank Adaptation structure, we employ a residual approach to fine-tune the frozen pre-trained parameter matrices for any weight matrix in the Multi-Head Attention (MHA) and Feed-Forward Network (FFN) modules. (2) Similarly, in the LoRA framework, we utilize dynamically generated down-projection and up-projection matrices instead of their counterparts applied to the \mathbf{W}_q and \mathbf{W}_v .

trix \mathbf{Q} is defined as:

$$\begin{bmatrix} q_0 & -q_1 & -q_2 & \cdots & -q_N \\ q_1 & 1 - \frac{q_1 q_1}{1+q_0} & -\frac{q_2 q_1}{1+q_0} & \cdots & -\frac{q_N q_1}{1+q_0} \\ q_2 & -\frac{q_1 q_2}{1+q_0} & 1 - \frac{q_2 q_2}{1+q_0} & \cdots & -\frac{q_N q_2}{1+q_0} \\ \vdots & \vdots & \vdots & \ddots & \vdots \\ q_i & -\frac{q_1 q_i}{1+q_0} & -\frac{q_2 q_i}{1+q_0} & \cdots & -\frac{q_N q_i}{1+q_0} \\ \vdots & \vdots & \vdots & \ddots & \vdots \\ q_N & -\frac{q_1 q_N}{1+q_0} & -\frac{q_2 q_N}{1+q_0} & \cdots & 1 - \frac{q_N q_N}{1+q_0} \end{bmatrix}, \quad (5)$$

the column vectors of \mathbf{Q} are strictly orthogonal to each other when using the normalization $\sum_{i=1}^N |q_i|^2 = 1$. To enhance the flexibility of the model's capacity, we do not strictly adhere to this normalization, allowing the column vectors of the matrix \mathbf{Q} to be approximately orthogonal.

Based on this design, we can derive the LoRA alternative as follows:

$$\mathbf{X}_{\text{FT}}^{(l-1)} = \mathbf{X}^{(l-1)} (\mathbf{W}^{(l)} + \text{AO}(\vec{q}_{\text{down}}) \text{AO}(\vec{q}_{\text{up}})^\top), \quad (6)$$

where $\mathbf{W}^{(l)}$ is $\mathbf{W}_q^{(l)}$ or $\mathbf{W}_v^{(l)}$. Similarly, we can derive a scheme for combining AOFT with Adapter-based method, as follows:

$$\begin{aligned} \mathbf{X}_{\text{FT}}^{(l-1)} &= \text{MHA}(\mathbf{X}^{(l-1)}) \text{AO}(\vec{q}_{\text{down}}^{\text{MHA}}) \text{AO}(\vec{q}_{\text{up}}^{\text{MHA}})^\top, \\ \mathbf{X}_{\text{FT}}^{(l)} &= \text{FFN}(\mathbf{X}_{\text{FT}}^{(l-1)}) \text{AO}(\vec{q}_{\text{down}}^{\text{FFN}}) \text{AO}(\vec{q}_{\text{up}}^{\text{FFN}})^\top. \end{aligned} \quad (7)$$

Their AOFT structures are shown in Fig. 3, and we can observe that the degree distribution of any two column vectors within the fine-tuned projection matrix reveals approximate orthogonality, as shown in Fig. 4.

Despite the differences between the prompt structure of VPT and the bottleneck structure of LoRA and Adapter, we also try to apply AOFT to the VPT approach. We replace the prompt part with a single matrix, as follows:

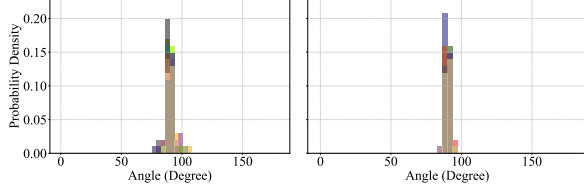
$$\mathbf{X}_{\text{FT}}^{(l-1)} = \begin{pmatrix} \mathbf{X}^{(l-1)} \\ \text{AO}(\vec{q}_{\text{prompt}})^\top \end{pmatrix} \mathbf{W}^{(l)} + \vec{b}^{(l)\top}, \quad (8)$$

and the angle distribution of any two column vectors of prompt matrix is illustrated in Fig. 7 of Section 4.3.

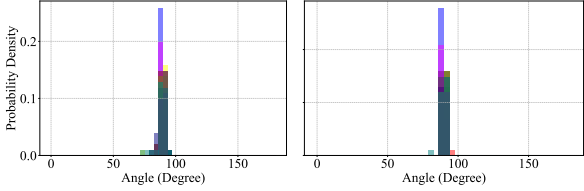
3.3. Upper Bound of Generalization Error for AOFT

Generalization error reflects the generalization capability of a model. If one model has a smaller generalization error than another, then the model is considered effective. In fact, the generalization error represents the expected risk of the learned model.

In this section, we utilize Rademacher Complexity [6] to define the upper bound of generalization error of models:



(a) The angle distribution of any two column vectors of down-projection matrix in LoRA with projection matrix in LoRA with AOFT.



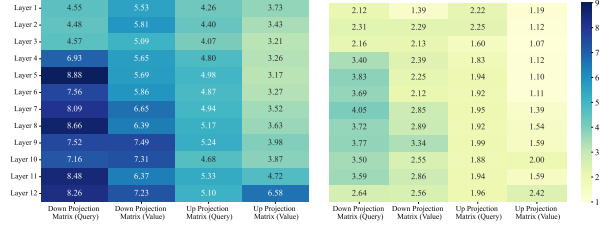
(c) The angle distribution of any two column vectors of up-projection matrix in Adapter with projection matrix in Adapter with AOFT.

Figure 4. Down/up-projection matrices trained through using the combination of AOFT with LoRA, Adapter methods exhibit a distribution of angles between pairs of vectors that are concentrated around 90 degrees, indicating that these vectors are approximately pairwise orthogonal to each other. Specifically, (a) and (b) show the angle distribution of any two column vectors in fine-tuned down/up-projection matrices of LoRA; (c) and (d) demonstrate the counterparts of Adapter. These figures are all obtained from models trained on the dtd dataset. Their legends can be found in Appendix A.

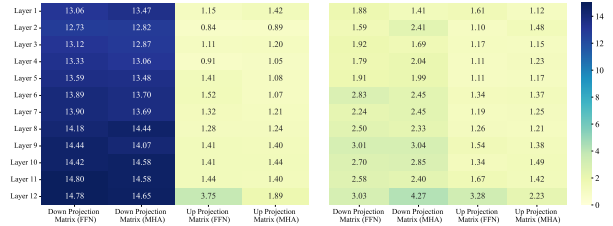
$$\begin{aligned}
& \mathbb{E}_{\xi \in \{\pm 1\}^m} \left[\frac{1}{m} \sup_{\|\mathbf{W}\| \leq \gamma} \left\| \sum_{i=1}^m \xi_i \mathbf{W} \vec{x}_i \right\| \right] \\
&= \mathbb{E}_{\xi \in \{\pm 1\}^m} \left[\frac{1}{m} \sup_{\|\mathbf{W}\| \leq \gamma} \left\| \mathbf{W} \sum_{i=1}^m \xi_i \vec{x}_i \right\| \right] \\
&\leq \mathbb{E}_{\xi \in \{\pm 1\}^m} \left[\frac{1}{m} \sup_{\|\mathbf{W}\| \leq \gamma} \|\mathbf{W}\| \left\| \sum_{i=1}^m \xi_i \vec{x}_i \right\| \right],
\end{aligned} \tag{9}$$

where m represents the number of samples; \vec{x}_i denotes the sample features; \mathbf{W} is the weight matrix; ξ_i is a Rademacher variable; and γ stands for the L2-norm of \mathbf{W} . Hence, the magnitude of γ determines the upper bound of the generalization error. As γ increases, the upper bound of the generalization error becomes larger; conversely, as γ decreases, the upper bound of the generalization error becomes smaller.

In our method, the L2-norms $\|\mathbf{W}_{\text{down}}\|$ and $\|\mathbf{W}_{\text{up}}\|$ of AOFT are significantly smaller than that of the LoRA and Adapter methods, as illustrated in Fig. 5. Consequently, the upper bound of the generalization error for AOFT is much lower than that of the Lora and Adapter methods, demonstrating that AOFT possesses superior generalization capability.



(a) The L2-norms of down/up-projection matrices in LoRA.



(c) The L2-norm of down/up-projection matrices in Adapter.

(d) The L2-norm of down/up-projection matrices in Adapter with AOFT.

4. Experiments

We conducted a comprehensive series of experiments, demonstrating that AOFT is a robust and reliable method with plug-and-play functionality. The detailed experimental setups and additional results are presented in the supplementary materials.

4.1. Experiments Setting

Datasets. Following the previous works [2, 11, 12, 15], we utilized two visual adaptation benchmarks to assess the effectiveness of our method: Fine-Grained Visual Classification (FGVC) and VTAB-1k [33], encompassing a total of 24 datasets. FGVC comprises five Fine-Grained Visual Classification datasets: *CUB-200-2011* [31], *NABirds* [29], *Oxford Flowers* [23], *Stanford Dogs* [13], and *Stanford Cars* [5]. Meanwhile, VTAB-1k includes a diverse set of datasets across various categories. These datasets are specifically tailored to tackle the intricate task of distinguishing between visually similar subcategories within broader categories, thereby rendering the challenge more demanding and intricate. The VTAB-1k benchmark showcases an impressive array of 19 diverse visual classification tasks, categorized into three broad groups: *Natural*, *Specialized*, and *Structured*. *Natural* focuses on images captured by standard cameras, representing natural scenes. *Specialized* features images taken by specialized equipment, such as remote sensing and medical imaging devices. *Structured* includes synthesized images from simulated environments, covering tasks like object counting and 3D depth prediction. Each VTAB-1k task comprises 1,000

Table 1. Performance comparison of Adapter, LoRA and VPT, where AOFT is integrated into these PEFT methods on the FGVC dataset. All experiments are conducted using ViT-B/16 pre-trained on ImageNet-21K as the backbone. The best results are shown in **bold**.

Methods \ Datasets	CUB-200-2011	NABirds	Oxford Flowers	Stanford Dogs	Stanford Cars	Mean Total	Params. (M)
Full fine-tuning	87.3	82.7	98.8	89.4	84.5	88.5	85.98
Linear probing	85.3	75.9	97.9	86.2	51.3	79.3	0.18
Adapter [9]	87.1	84.3	98.5	89.8	68.6	85.7	0.41
Adapter+AOFT	88.6	83.7	99.4	89.8	83.0	88.9	0.20
Adapter+AOFT*	89.0	84.5	99.5	92.0	85.2	90.1	0.20
LoRA [10]	88.3	85.6	99.2	91.0	83.2	89.5	0.44
LoRA+AOFT	88.8	84.2	99.4	92.0	85.1	89.9	0.22
LoRA+AOFT*	88.4	84.2	99.5	92.0	85.0	89.8	0.22
VPT-Shallow [11]	86.7	78.8	98.4	90.7	68.7	84.7	0.25
VPT-Shallow+AOFT(dim=64)	88.9	81.5	99.8	92.4	61.7	84.0	0.18
VPT-Deep [11]	88.5	84.2	99.0	90.2	83.6	89.1	0.85
VPT-Deep+AOFT(dim=768)	88.7	82.8	99.5	91.5	84.1	89.5	0.15

training samples. The relevant content can be found in the Appendix B.

Baselines and existing PEFT methods. To evaluate the performance of AOFT, we conducted a comparative analysis by integrating it with two baseline methods and three well-known PEFT approaches including LoRA, Adapter, and VPT-Shallow/Deep. The two baseline methods are: (1) Full Fine-Tuning, which involves updating all parameters of the pre-trained model using training data from the downstream task, and (2) Linear Probing, which entails training only a linear classification head on the downstream task while keeping the remaining pre-trained parameters frozen.

Our PEFT methods. The AOFT methods are denoted as Adapter+AOFT (Eq. 7), LoRA+AOFT (Eq. 6), VPT-Shallow+AOFT (Eq. 8) and VPT-Deep+AOFT (Eq. 8). To enhance the flexibility of our method, we introduce a learnable scaling vector $\tilde{\lambda}$ to modulate the down/up-projection matrix, forming AOFT* for both Adapter and LoRA. Specifically, AOFT* is defined as $(\mathbf{W}_{\text{down}} \odot \tilde{\lambda}^{\top})\mathbf{W}_{\text{up}}$, where \odot denotes element-wise multiplication. Since our approach does not introduce additional parameters when increasing the bottleneck dimension, we can dynamically adjust the bottleneck size for different downstream tasks, ensuring optimal performance for each setting. The corresponding results are reported in the AOFT* row of Tab. 2.

Implementation details. During the training phase, we employed the default data augmentation strategy. For the FGVC datasets, images were randomly resized and cropped to 224×224 pixels, and a random horizontal flip was applied to augment the data. For the VTAB-1k datasets, we adhered to the default settings and directly resized the images to 224×224 pixels. To fine-tune the models, we employed the AdamW optimizer for 100 epochs. Additionally, we managed the learning rate using a cosine decay strategy, ensuring effective model training. All experiments are conducted using the PyTorch framework on an NVIDIA A800 GPU with 80 GB of memory.

4.2. Experimental Comparisons

In this section, we integrate our method with various backbones and provide a quantitative comparison to evaluate its effectiveness.

Comparison with the existing PEFT methods. We evaluate the AOFT integrate state-of-the-art PEFT approaches on two benchmarks: FGVC and VTAB-1k. When applied to Adapter, VPT, LoRA, OFT and GOFT. More orthogonal fine-tuning practices have been conducted on language models, so we do not compare with them. Our method consistently demonstrates significant performance improvements, as shown in Tables Tab. 1 and Tab. 2. Notably, these enhancements are achieved while reducing the parameter count by more than half. In particular, on the VTAB-1k [34] dataset, integrating AOFT with the VPT approach results in an average performance gain of 1.3% across 19 datasets, while simultaneously reducing the parameter count by an order of magnitude. Furthermore, for the LoRA method, AOFT[†] achieves 1.8% improvement in performance. These results demonstrate the potential of AOFT to facilitate the fine-tuning of foundational models under resource-constrained conditions.

Experiments on larger-scale ViT backbones. In addition to evaluating our method on the ViT-B backbone, we further conducted experiments on larger backbones, ViT-L and ViT-H [4], to assess the effectiveness of AOFT when applied to more complex and large-scale architectures. As shown in Tab. 3, models integrated with AOFT consistently outperform their respective baselines, demonstrating that AOFT maintains strong performance even when applied to larger backbone networks.

Experiments on hierarchical Vision Transformers. To further explore the scalability of AOFT, we extend our method to the Swin Transformer [18], a hierarchical vision model that partitions the input into multiple stages, with each stage consisting of transformer modules operating at a fixed and unique feature resolution. As shown in Tab. 4, the integration of AOFT with LoRA achieves state-of-the-art

Table 2. Performance comparison of Adapter, LoRA, VPT, OFT and GOFT where AOFT is integrated into these PEFT methods on the VTAB-1k dataset. All experiments are conducted using ViT-B/16 pre-trained on ImageNet-21K as the backbone. The best results are shown in **bold**. AOFT* is defined as $(\mathbf{W}_{\text{down}} \odot \tilde{\mathbf{X}}^T) \mathbf{W}_{\text{up}}$, AOFT[†] indicates results using different bottleneck structures.

Methods	Datasets		Natural							Specialized					Structed										Mean Total	Params.(M)
	CIFAR-100	Caltech101	DTD	Flowers102	Pets	SVNH	Sun397	Mean	Camelyon	EuroSAT	Resisc45	Retinopathy	Mean	Clevr-Count	Clevr-Dist	DMLab	KITTI-Dist	dSpr-Loc	dSpr-Ori	sNORB-Azim	sNORB-Ele	Mean				
Full fine-tuning	68.9	87.7	64.3	97.2	86.9	87.4	38.8	75.9	79.7	95.7	84.2	73.9	83.4	56.3	58.6	41.7	65.5	57.5	46.7	25.7	29.1	47.6	65.6	85.80		
Linear probing	63.4	85.0	63.2	97.0	86.3	36.6	51.0	68.9	78.7	87.5	68.6	74.0	77.2	34.3	30.6	33.2	55.4	12.5	20.0	9.6	19.2	26.9	52.9	0.04		
VPT-Shallow [11]	77.7	86.9	62.6	97.5	87.3	74.5	51.2	76.8	78.2	92.0	75.6	72.9	79.7	50.0	58.6	40.5	67.1	68.7	36.1	20.2	34.1	47.0	64.8	0.11		
VPT-Shallow+AOFT(dim=64)	71.8	90.7	71.8	99.0	91.3	75.6	56.7	79.5	81.5	92.6	81.3	74.3	82.4	53.0	59.0	44.2	76.4	58.6	40.7	22.5	28.1	47.8	66.8	0.05		
VPT-Deep [11]	78.8	90.8	65.8	98.0	88.3	78.1	49.6	78.5	81.8	96.1	83.4	68.4	82.4	68.5	60.0	46.5	72.8	73.6	47.9	32.9	37.8	55.0	69.4	0.60		
VPT-Deep+AOFT(dim=768)	70.7	92.9	70.1	99.2	91.5	87.0	50.8	80.3	84.9	93.9	83.9	76.1	84.7	65.6	61.2	48.6	82.3	72.1	49.2	27.9	36.0	55.4	70.7	0.05		
Adapter [9]	69.2	90.1	68.0	98.8	89.9	82.8	54.3	79.0	84.0	94.9	81.9	75.5	84.1	80.9	65.3	48.6	78.3	74.8	48.5	29.9	41.6	58.5	71.4	0.16		
Adapter+AOFT	64.9	93.3	71.6	99.1	90.9	85.5	49.7	79.3	83.4	94.2	83.3	76.0	84.2	79.4	63.2	47.6	81.3	87.0	54.7	26.3	45.4	60.6	72.5	0.06		
Adapter+AOFT*	74.6	93.9	71.4	99.4	90.1	78.0	57.1	81.4	82.0	94.0	84.1	75.6	83.9	78.8	62.5	48.5	79.6	84.6	54.3	24.1	42.7	59.4	72.7	0.06		
LoRA [10]	67.1	91.4	69.4	98.8	90.4	85.3	54.0	79.5	84.9	95.3	84.4	73.6	84.6	82.9	69.2	49.8	78.5	75.7	47.1	31.0	44.0	59.8	72.3	0.29		
LoRA+AOFT	73.6	92.6	71.1	99.3	91.3	85.3	56.9	81.4	84.7	94.8	83.7	75.6	84.7	76.7	63.2	48.7	81.0	82.2	53.1	26.9	45.1	59.6	72.9	0.08		
LoRA+AOFT*	74.0	91.0	72.7	99.3	89.3	80.6	56.8	80.5	84.9	94.6	82.7	75.6	84.7	71.4	57.5	42.7	82.0	83.4	53.9	22.6	44.5	57.3	71.5	0.08		
VeRA [14]	74.5	92.7	71.5	99.2	90.0	84.8	56.2	81.3	82.5	92.0	81.5	74.7	82.7	71.5	61.3	49.3	79.5	78.7	42.9	30.5	42.4	57.0	71.4	0.03		
OFT [24]	65.1	88.4	70.0	96.5	88.7	88.5	45.7	77.6	86.7	96.6	85.5	77.0	86.5	79.7	67.6	50.2	77.8	78.5	50.8	30.9	40.5	59.5	71.8	0.15		
DoRA [16]	66.1	93.1	68.8	97.0	89.9	87.2	56.4	79.8	83.1	94.5	80.8	75.2	83.4	79.1	62.1	48.0	80.6	83.1	51.8	33.2	44.0	60.2	72.3	0.19		
GOFT [21]	71.5	90.9	68.8	96.2	88.6	81.7	57.2	79.3	85.6	96.5	84.6	78.7	86.4	80.5	70.7	51.8	78.5	77.3	49.2	28.7	40.3	59.6	72.5	0.02		
MoIL [20]	71.7	92.8	69.6	99.1	89.8	84.2	56.0	80.5	84.7	94.9	82.3	74.6	84.1	79.5	62.7	49.1	81.6	81.5	48.4	36.9	47.5	60.9	73.0	0.63		
RepAdapter _{attn} [19]	70.7	91.6	72.5	99.1	91.3	88.5	54.2	81.1	84.1	95.7	85.1	74.6	84.9	81.6	69.1	50.4	81.9	79.5	45.6	34.6	41.9	60.6	73.3	0.11		
Adapter _{r=1} [27]	85.4	92.4	73.1	99.1	91.3	83.1	58.1	83.2	87.2	96.6	85.3	72.6	85.4	80.7	60.6	50.9	79.9	83.3	55.6	27.1	43.0	60.1	74.0	0.07		
LoRA+AOFT†	74.2	93.4	77.7	99.4	91.5	85.5	57.3	82.0	86.3	95.2	84.0	75.8	85.3	78.9	63.1	51.2	82.6	83.6	53.9	31.9	47.3	57.3	74.1	0.08		

Table 3. Performance comparison on VTAB-1k using ViT-Large and ViT-Huge pre-trained on ImageNet-21k as the backbone. The notation "(·)" indicates the number of tasks in the subgroup. Detailed results are presented in Appendix C. The best results are shown in **bold**.

Methods	(a) ViT-Large					(b) ViT-Huge				
	Natural (7)	Specialized (4)	Structed (8)	Mean	Params.(M)	Natural (7)	Specialized (4)	Structed (8)	Mean	Params.(M)
Full fine-tuning	74.7	83.8	48.1	65.4	303.40	70.9	83.6	46.0	63.1	630.90
Linear probing	70.9	69.1	25.8	51.5	0.05	67.9	79.0	26.1	52.7	0.06
Adapter [9]	68.6	73.5	29.0	52.9	2.38	68.1	76.4	24.5	51.5	5.78
Adapter+AOFT*	70.7	77.0	44.4	60.9	0.10	77.7	81.8	37.1	61.5	0.17
LoRA [10]	81.4	85.0	57.3	72.0	0.74	77.1	83.5	55.4	69.3	1.21
LoRA+AOFT*	83.3	85.9	60.2	74.3	0.15	78.8	83.8	58.3	71.3	0.20

Table 4. Performance comparison on VTAB-1k using Swin Transformer pre-trained on ImageNet-21k as the backbone. "(·)" indicates the number of tasks in the subgroup. Detailed results are presented in Appendix C. The best results are shown in **bold**.

Methods	Natural (7)	Specialized (4)	Structed (8)	Mean Total	Params.(M)
Full fine-tuning	79.1	86.2	59.7	72.4	86.80
Linear probing	73.5	80.8	33.5	58.2	0.05
MLP-4 [11]	70.6	80.7	31.2	57.7	4.04
Partial [11]	73.1	81.7	35.0	58.9	12.65
Bias [32]	74.2	80.1	42.4	62.1	0.25
VPT-Shallow [11]	79.9	82.5	37.8	62.9	0.05
VPT-Deep [11]	76.8	84.5	53.4	67.7	0.22
ARC [2]	79.0	86.6	59.9	72.6	0.27
RLRR [3]	81.3	86.7	59.0	73.0	0.41
LoRA+AOFT*	82.3	86.8	60.6	73.3	0.14

performance. Compared to ARC, which shares a low-rank matrix, our method reduces the parameter count by half while achieving 0.7% performance improvement, demonstrating its robustness in adapting to foundation models.

4.3. Ablation Studies

In this section, we conduct a detailed ablation study to investigate the underlying mechanisms of AOFT, examining its impact across different model positions and the effect of varying bottleneck dimensionality on performance across

the selected benchmarks.

Effect of combining AOFT and Low-Rank adaptation.

To evaluate the adaptive effects of AOFT across different model components, we applied it to various positions, including multiple components within MHA and FFN. Our findings align with the conclusions from the original LoRA paper, where applying LoRA to only the query \mathbf{W}_q and value \mathbf{W}_v matrices yields performance comparable to applying it to all components. Similarly, AOFT achieves competitive results under the same setting when adapters are applied to the feedforward neural network \mathbf{W}_{FC1} and \mathbf{W}_{FC2} , further validating its effectiveness in low-rank adaptation. This demonstrates that AOFT can be seamlessly incorporated into LoRA, further enhancing its adaptability and efficiency in low-rank adaptation.

Effect of bottleneck dimension on the performance of AOFT.

Fig. 6 illustrates the impact of bottleneck dimensionality on the performance of AOFT within low-rank structures. Previous studies [7, 25, 26, 30] have shown that different tasks require varying matrix dimensions. To systematically investigate this effect, we varied the bottleneck dimension in our experiments. Notably, our approach con-

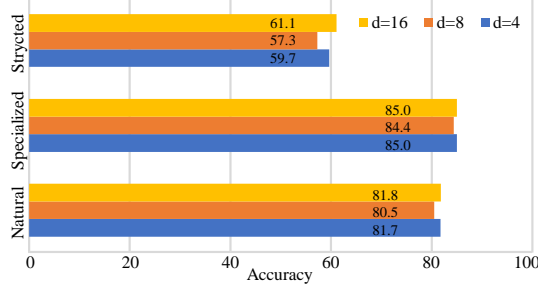


Figure 6. Ablation study on the impact of different bottleneck dimensions of adaptive matrices in AOFT. The bar chart represents the Top-1 Test Accuracy. Each bar represents the average accuracy of predictions for that particular type of dataset.

Table 5. AOFT is used to replace the down/up-projection matrices, and the experiment was conducted on ViT-B/16 backbone and VTAB-1k dataset. According to previous experiments, AOFT is applied to the $\{\mathbf{W}_q, \mathbf{W}_v\}$ and $\{\mathbf{W}_{FC1}, \mathbf{W}_{FC2}\}$ matrices, and different bottleneck dimensions were set for ablation experiments. The best results are shown in **bold**.

Methods	Natural (7)	Specialized (4)	Strucetd (8)	Mean Total	Params.(M)
LoRA($\mathbf{W}_q, \mathbf{W}_v$)	79.5	84.6	59.8	72.3	0.29
LoRA+AOFT($\mathbf{W}_q, \mathbf{W}_v$)	81.7	85.0	59.7	73.1	0.08
LoRA+AOFT($\mathbf{W}_q, \mathbf{W}_v, \mathbf{W}_{FC1}, \mathbf{W}_{FC2}$)	81.4	85.3	60.6	73.4	0.16
Adapter(\mathbf{W}_{FFN})	79.0	84.1	58.5	71.4	0.16
Adapter+AOFT(\mathbf{W}_{FFN})	81.5	85.2	59.5	73.0	0.06
Adapter+AOFT($\mathbf{W}_{FFN}, \mathbf{W}_{MHA}$)	80.7	86.2	60.9	73.5	0.08

Table 6. Comparison of the L2-norms of prompt matrices between VPT-Deep and VPT-Deep+AOFT. The best results are shown in **bold**.

Methods	Layer 1	Layer 2	Layer 3	Layer 4	Layer 5	Layer 6
VPT-Deep [11]	7.41	6.17	6.02	5.08	5.36	5.01
VPT-Deep+AOFT	1.09	1.04	1.07	1.04	1.04	1.05

Methods	Layer 7	Layer 8	Layer 9	Layer 10	Layer 11	Layer 12
VPT-Deep [11]	4.28	3.77	3.09	2.67	2.15	3.03
VPT-Deep+AOFT	1.04	1.03	1.10	1.04	1.04	1.16

structs matrices from a single vector, enabling the generation of an arbitrary number of approximately orthogonal column vectors. This property allows for flexible adjustment of dimensionality without increasing the total number of parameters. As observed in the figure, AOFT demonstrates significant potential, highlighting its advantages and broader applicability. This suggests that AOFT can effectively adapt to different task requirements while maintaining parameter efficiency, making it a promising approach for low-rank adaptation.

The L2-norms and angle distribution of VPT integrated with AOFT. In Eq.(9), we provide a general derivation of the impact of the L2-norm on generalization, which suggests that larger norms lead to poorer generalization performance. Furthermore, the experiments in Section 4.2 have already demonstrated that our method effectively improves performance when applied to VPT. The result is show in Tab. 2. To further investigate this effect, we analyze the behavior of the L2-norm across different layers to illustrate the

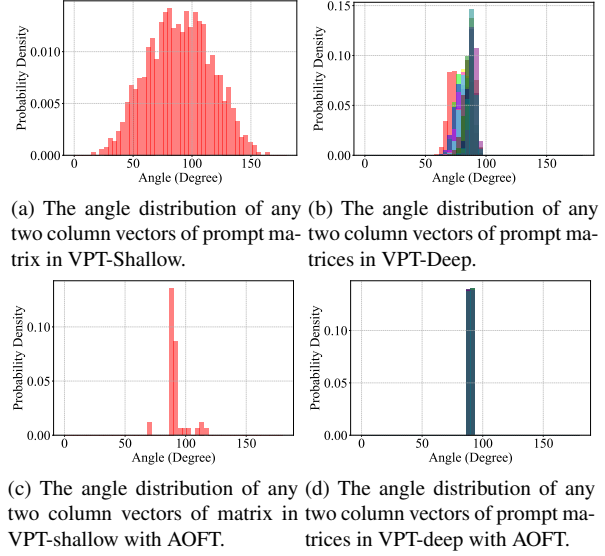


Figure 7. Comparison of the angle distribution between any two column vectors within the prompt matrices of VPT and those enhanced with AOFT. These results are all obtained from models trained on the dtd dataset. Their legends can be found in Appendix A.

influence of AOFT on existing PEFT methods, with the results presented in Tab. 6. Additionally, Fig. 7 shown the angular distribution between arbitrary column vectors within the prompt matrix when applying AOFT to VPT. These findings indicate that the approximate orthogonality strategy helps mitigate generalization errors, thereby improving overall model performance.

5. Conclusions

In this work, we propose the Approximately Orthogonal Fine-Tuning (AOFT) strategy, which generates approximately orthogonal vectors for down/up-projection matrices using a single learnable vector, aligning their properties with the backbone. Specifically, we replace the down- and up-projection matrices in prevalent methods like LoRA and Adapter with matrices that have approximately orthogonal columns. This strategy is linked to reduced generalization error and enhanced model capability. Experimental results across various image classification downstream tasks confirm the efficacy of AOFT in enhancing generalization capability, achieving competitive performance.

6. Acknowledgments and Disclosure of Funding

This work was supported by Major Science and Technology Innovation Special Project Plan of Xianyang (Program No. L2024-ZDKJ-ZDGG-GY-0010) and Natural Science Basic Research Program of Shaanxi (Program No.2024JC-YBMS-464).

References

- [1] Tim Dettmers, Artidoro Pagnoni, Ari Holtzman, and Luke Zettlemoyer. Qlora: Efficient finetuning of quantized llms. *Advances in neural information processing systems*, 36: 10088–10115, 2023. 1
- [2] Wei Dong, Dawei Yan, Zhijun Lin, and Peng Wang. Efficient adaptation of large vision transformer via adapter recomposing. In *Thirty-seventh Conference on Neural Information Processing Systems*, 2023. 3, 5, 7
- [3] Wei Dong, Xing Zhang, Bihui Chen, Dawei Yan, Zhijun Lin, Qingsen Yan, Peng Wang, and Yang Yang. Low-rank rescaled vision transformer fine-tuning: A residual design approach. In *Proceedings of the IEEE/CVF Conference on Computer Vision and Pattern Recognition*, pages 16101–16110, 2024. 3, 7
- [4] Alexey Dosovitskiy, Lucas Beyer, Alexander Kolesnikov, Dirk Weissenborn, Xiaohua Zhai, Thomas Unterthiner, Mostafa Dehghani, Matthias Minderer, Georg Heigold, Sylvain Gelly, et al. An image is worth 16x16 words: Transformers for image recognition at scale. In *International Conference on Learning Representations*, 2020. 1, 3, 6
- [5] Timnit Gebru, Jonathan Krause, Yilun Wang, Duyun Chen, Jia Deng, and Li Fei-Fei. Fine-grained car detection for visual census estimation. In *Proceedings of the AAAI Conference on Artificial Intelligence*, 2017. 5, 2
- [6] Vishal Goar and Nagendra Singh Yadav. Foundations of machine learning. In *Intelligent Optimization Techniques for Business Analytics*, pages 25–48. IGI Global, 2024. 4
- [7] Yoav Goldberg. *Neural network methods in natural language processing*. Morgan & Claypool Publishers, 2017. 7
- [8] Gene H Golub and Charles F Van Loan. *Matrix computations*. JHU press, 2013. 2
- [9] Neil Houlsby, Andrei Giurgiu, Stanislaw Jastrzebski, Bruna Morroni, Quentin De Laroussilhe, Andrea Gesmundo, Mona Attariyan, and Sylvain Gelly. Parameter-efficient transfer learning for nlp. In *International Conference on Machine Learning*, pages 2790–2799. PMLR, 2019. 1, 2, 6, 7, 3
- [10] Edward J Hu, Phillip Wallis, Zeyuan Allen-Zhu, Yuanzhi Li, Shean Wang, Lu Wang, Weizhu Chen, et al. Lora: Low-rank adaptation of large language models. In *International Conference on Learning Representations*, 2021. 1, 2, 6, 7, 3
- [11] Menglin Jia, Luming Tang, Bor-Chun Chen, Claire Cardie, Serge Belongie, Bharath Hariharan, and Ser-Nam Lim. Visual prompt tuning. In *European Conference on Computer Vision*, pages 709–727. Springer, 2022. 1, 3, 5, 6, 7, 8, 2
- [12] Shibo Jie and Zhi-Hong Deng. Fact: Factor-tuning for lightweight adaptation on vision transformer. In *Proceedings of the AAAI Conference on Artificial Intelligence*, pages 1060–1068, 2023. 5
- [13] Aditya Khosla, Nityananda Jayadevaprakash, Bangpeng Yao, and Fei-Fei Li. Novel dataset for fine-grained image categorization: Stanford dogs. In *Proc. CVPR workshop on fine-grained visual categorization (FGVC)*. Citeseer, 2011. 5, 2
- [14] Dawid J Kopiczko, Tijmen Blankevoort, and Yuki M Asano. Vera: Vector-based random matrix adaptation. *arXiv preprint arXiv:2310.11454*, 2023. 1, 2, 7
- [15] Dongze Lian, Daquan Zhou, Jiashi Feng, and Xinchao Wang. Scaling & shifting your features: A new baseline for efficient model tuning. *Advances in Neural Information Processing Systems*, 35:109–123, 2022. 5
- [16] Shih-Yang Liu, Chien-Yi Wang, Hongxu Yin, Pavlo Molchanov, Yu-Chiang Frank Wang, Kwang-Ting Cheng, and Min-Hung Chen. Dora: Weight-decomposed low-rank adaptation. In *Forty-first International Conference on Machine Learning*, 2024. 7
- [17] Weiyang Liu, Zeju Qiu, Yao Feng, Yuliang Xiu, Yuxuan Xue, Longhui Yu, Haiwen Feng, Zhen Liu, Juyeon Heo, Songyou Peng, et al. Parameter-efficient orthogonal finetuning via butterfly factorization. *arXiv preprint arXiv:2311.06243*, 2023. 3
- [18] Ze Liu, Yutong Lin, Yue Cao, Han Hu, Yixuan Wei, Zheng Zhang, Stephen Lin, and Baining Guo. Swin transformer: Hierarchical vision transformer using shifted windows. In *Proceedings of the IEEE/CVF international conference on computer vision*, pages 10012–10022, 2021. 6
- [19] Gen Luo, Minglang Huang, Yiyi Zhou, Xiaoshuai Sun, Guannan Jiang, Zhiyu Wang, and Rongrong Ji. Towards efficient visual adaption via structural re-parameterization. *arXiv preprint arXiv:2302.08106*, 2023. 7
- [20] Gen Luo, Yiyi Zhou, Minglang Huang, Tianhe Ren, Xiaoshuai Sun, and Rongrong Ji. Moil: Momentum imitation learning for efficient vision-language adaptation. *IEEE Transactions on Pattern Analysis and Machine Intelligence*, 2024. 7
- [21] Xinyu Ma, Xu Chu, Zhibang Yang, Yang Lin, Xin Gao, and Junfeng Zhao. Parameter efficient quasi-orthogonal finetuning via givens rotation. *arXiv preprint arXiv:2404.04316*, 2024. 3, 7
- [22] István Mayer. *Simple theorems, proofs, and derivations in quantum chemistry*. Springer Science & Business Media, 2013. 3
- [23] Maria-Elena Nilsback and Andrew Zisserman. Automated flower classification over a large number of classes. In *2008 Sixth Indian conference on computer vision, graphics & image processing*, pages 722–729. IEEE, 2008. 5, 2
- [24] Zeju Qiu, Weiyang Liu, Haiwen Feng, Yuxuan Xue, Yao Feng, Zhen Liu, Dan Zhang, Adrian Weller, and Bernhard Schölkopf. Controlling text-to-image diffusion by orthogonal finetuning. *Advances in Neural Information Processing Systems*, 36:79320–79362, 2023. 3, 7
- [25] Jürgen Schmidhuber. Deep learning in neural networks: An overview. *Neural networks*, 61:85–117, 2015. 7
- [26] Haobin Shi, Zhiqiang Lin, Kao-Shing Hwang, Shike Yang, and Jialin Chen. An adaptive strategy selection method with reinforcement learning for robotic soccer games. *IEEE Access*, 6:8376–8386, 2018. 7
- [27] Jan-Martin O Steitz and Stefan Roth. Adapters strike back. In *Proceedings of the IEEE/CVF Conference on Computer Vision and Pattern Recognition*, pages 23449–23459, 2024. 7
- [28] Lloyd N Trefethen and David Bau. *Numerical linear algebra*. SIAM, 2022. 2

- [29] Grant Van Horn, Steve Branson, Ryan Farrell, Scott Haber, Jessie Barry, Panos Ipeirotis, Pietro Perona, and Serge Belongie. Building a bird recognition app and large scale dataset with citizen scientists: The fine print in fine-grained dataset collection. In *Proceedings of the IEEE conference on computer vision and pattern recognition*, pages 595–604, 2015. [5](#), [2](#)
- [30] A Vasuki and S Govindaraju. Deep neural networks for image classification. In *Deep Learning for Image Processing Applications*, pages 27–49. IOS Press, 2017. [7](#)
- [31] Catherine Wah, Steve Branson, Peter Welinder, Pietro Perona, and Serge Belongie. The caltech-ucsd birds-200-2011 dataset. 2011. [5](#), [2](#)
- [32] Elad Ben Zaken, Yoav Goldberg, and Shauli Ravfogel. Bitfit: Simple parameter-efficient fine-tuning for transformer-based masked language-models. In *Proceedings of the 60th Annual Meeting of the Association for Computational Linguistics (Volume 2: Short Papers)*, pages 1–9, 2022. [7](#), [3](#)
- [33] Xiaohua Zhai, Joan Puigcerver, Alexander Kolesnikov, Pierre Ruysen, Carlos Riquelme, Mario Lucic, Josip Djolonga, Andre Susano Pinto, Maxim Neumann, Alexey Dosovitskiy, et al. A large-scale study of representation learning with the visual task adaptation benchmark. *arXiv preprint arXiv:1910.04867*, 2019. [5](#), [2](#)
- [34] Xiaohua Zhai, Joan Puigcerver, Alexander Kolesnikov, Pierre Ruysen, Carlos Riquelme, Mario Lucic, Josip Djolonga, Andre Susano Pinto, Maxim Neumann, Alexey Dosovitskiy, et al. The visual task adaptation benchmark. 2019. [6](#)

Efficient Adaptation of Pre-trained Vision Transformer underpinned by Approximately Orthogonal Fine-Tuning Strategy

Supplementary Material

A. Angle Distribution

In the weights of the ViT-B/16 pre-trained model $\mathbf{W}_q, \mathbf{W}_k, \mathbf{W}_v, \mathbf{W}_o, \mathbf{W}_{FC1}, \mathbf{W}_{FC2}$. The distribution of pairwise angles between the column vectors in these weight matrices is shown in the Fig. 8. It can be observed that in the ViT model, the matrices are approximately orthogonal.

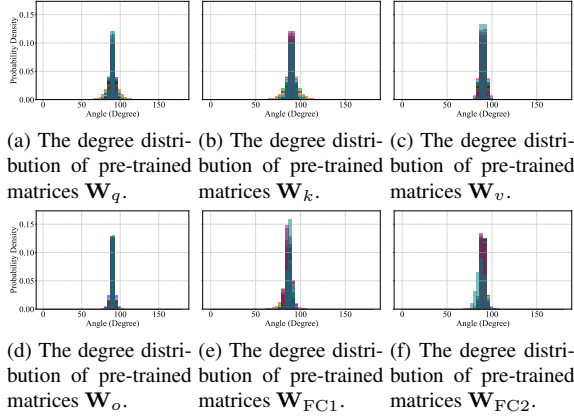


Figure 8. Illustration of approximate orthogonality among any two column vectors of weight matrices $\mathbf{W}_q, \mathbf{W}_k, \mathbf{W}_v, \mathbf{W}_o, \mathbf{W}_{FC1}, \mathbf{W}_{FC2}$ in the ViT-B model after training. The histogram represents the distribution of angles between any two column vectors within each weight matrix. Specifically, (a)-(f) represent approximate orthogonality in the pre-trained model. Their legends can be found in Fig. 9.

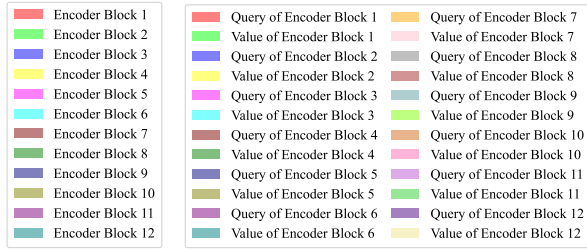


Figure 9. The legends for the bar chart.

Fig. 9 presents the legends for the statistical charts used throughout this paper. Fig. 9(a), specifically designed for charts that do not include the LoRA (Low-Rank Adaptation) method, clearly labels the line colors corresponding to different layers of the model, ensuring accurate differentiation among them.

Meanwhile, Fig. 9(b) is tailored for charts that incorporate the LoRA method. It distinctly showcases the line colors for different layers and matrices within those layers, facilitating precise differentiation.

B. Detailed Dataset Statistics

In this section, we provide a comprehensive overview of the visual adaptation classification tasks utilized in our study, presenting the specifics for both the Fine-Grained Visual Classification (FGVC) datasets and the Visual Task Adaptation Benchmark-1k (VTAB-1k) datasets. The dataset splits employed in our experiments follow the protocol established by VPT [11].

B.1. FGVC Datasets

The details of the FGVC datasets used in our study are summarized in Tab. 1. For each dataset, we report the number of classes, as well as the sizes of the training, validation, and test sets. These datasets are characterized by their fine-grained nature, requiring models to distinguish between subtle differences in appearance, making them ideal for evaluating the efficacy of visual adaptation techniques.

B.2. VTAB-1k Datasets

Similarly, the VTAB-1k datasets used in our experiments are detailed in Tab. 2. Again, we provide the number of classes and the sizes of the training, validation, and test sets for each dataset. The VTAB-1k benchmark is designed to assess the generalization capabilities of visual models across a diverse range of tasks, making it a valuable tool for evaluating the robustness and adaptability of our proposed methods.

By adhering to the dataset splits established by VPT [11], we ensure a fair and consistent comparison with existing work, facilitating the reproducibility and validation of our findings.

C. Experimental Details on Large-Scale, Huge-Scale, and Hierarchical ViT Backbones

In this section, we present the comprehensive results of our comparison among ViT-Large, ViT-Huge, and Swin-Base models, as discussed in Section 4. The detailed findings for each model are displayed in Tab. 3, 4, and 5, respectively.

Tab. 3 showcases the performance of the ViT-Large backbone across various tasks within the VTAB-1k benchmark. This table provides a thorough breakdown of the

Table 1. Dataset statistics for FGVC. “*” denotes the train/val split of datasets following the dataset setting in VPT [11].

Dataset	Description	Classes	Train size	Val size	Test size
CUB-200-2011 [31]	Fine-grained bird species recognition	200	5,394*	600*	5,794
NABirds [29]	Fine-grained bird species recognition	555	21,536*	2,393*	24,633
Oxford Flowers [23]	Fine-grained flower species recognition	102	1,020	1,020	6,149
Stanford Dogs [13]	Fine-grained dog species recognition	120	10,800*	1,200*	8,580
Stanford Cars [5]	Fine-grained car classificatio	196	7,329*	815*	8,041

Table 2. Dataset statistics for VTAB-1k [33].

Dataset	Description	Classes	Train size	Val size	Test size
CIFAR-100	Natural	100	800/1,000	200	10,000
Caltech101		102			6,084
DTD		47			1,880
Flowers102		102			6,149
Pets		37			3,669
SVHN		10			26,032
Sun397		397			21,750
Patch Camelyon	Specialized	2	800/1,000	200	32,768
EuroSAT		10			5,400
Resisc45		45			6,300
Retinopathy		5			42,670
Clevr/count	Structured	8	800/1,000	200	15,000
Clevr/distance		6			15,000
DMLab		6			22,735
KITTI/distance		4			711
dSprites/location		16			73,728
dSprites/orientation		16			73,728
SmallNORB/azimuth		18			12,150
SmallNORB/elevation		9			12,150

results, allowing for a detailed analysis of the model’s strengths and weaknesses in different contexts.

Similarly, Tab. 4 presents the results for the ViT-Huge backbone. By comparing these results to those of the ViT-Large model, we can gain insights into the benefits and trade-offs associated with scaling up the model size.

Lastly, Tab. 5 outlines the performance of the Swin-Base model, which adopts a hierarchical architecture. This table enables us to assess the effectiveness of hierarchical designs in comparison to the standard ViT architectures.

By examining these detailed results, we can draw meaningful conclusions regarding the performance characteristics of large-scale, huge-scale, and hierarchical ViT backbones. These insights contribute to a deeper understanding of the capabilities and limitations of these models in various visual adaptation tasks.

D. Orthogonality of Operators

In this work, a method is applied to generate multiple orthogonal basis from a vector to form a column of orthogonal matrices. The matrix \mathbf{Q} is derived from the matrix:

$$\begin{bmatrix} \cos \varphi & -x_1 \sin \varphi & \cdots & -x_i \sin \varphi \\ x_1 \sin \varphi & 1+x_1^2(\cos \varphi -1) & \cdots & x_i x_1(\cos \varphi -1) \\ x_2 \sin \varphi & x_1 x_2(\cos \varphi -1) & \cdots & x_i x_2(\cos \varphi -1) \\ \vdots & \vdots & \ddots & \vdots \\ x_i \sin \varphi & x_1 x_i(\cos \varphi -1) & \cdots & 1+x_i^2(\cos \varphi -1) \\ \vdots & \vdots & \ddots & \vdots \\ x_N \sin \varphi & x_1 x_N(\cos \varphi -1) & \cdots & x_i x_N(\cos \varphi -1) \end{bmatrix}, \quad (10)$$

let $\cos \varphi = q_0$ and $\sin \varphi = (\sum_{i=1}^N |q_i|^2)^{1/2}$, where $\sum_{i=1}^N |q_i|^2 = 1$, that means $x_i = \frac{q_i}{\sin \varphi} (i = 1, 2, \dots, N)$,

Table 3. This table is extended from ?? in Section 4 and describes the detailed experimental results of the performance comparison on VTAB-1k using ViT-Large pre-trained on ImageNet-21k as the backbone. Where Full fine-tuning and Linear probing are only used as controls and are not included in the bold comparison. The best results are shown in **bold**.

Methods \ Datasets	Natural								Specialized					Structred										Mean Total	Params.(M)
	CIFAR-100	Caltech101	DTD	Flowers102	Pets	SVNH	Sun397	Mean	Camelyon	EuroSAT	Resisc45	Retinopathy	Mean	Clevr-Count	Clevr-Dist	DMLab	KITTI-Dist	dSpr-Loc	dSpr-Ori	sNORB-Azim	sNORB-Ele	Mean			
Full fine-tuning	68.6	84.3	58.6	96.3	86.5	87.5	41.4	74.7	82.6	95.9	82.4	74.2	83.8	55.4	55.0	42.2	74.2	56.8	43.0	28.5	29.7	48.1	65.4	303.4	
Linear probing	72.2	86.4	63.6	97.4	85.8	38.1	52.5	70.9	76.9	87.3	66.6	45.4	69.1	28.2	28.0	34.7	54.0	10.6	14.2	14.6	21.9	25.8	51.5	0.05	
Adapter [9]	75.3	84.2	54.5	97.4	84.3	31.3	52.9	68.6	75.8	85.1	63.4	69.5	73.5	35.4	34.1	30.8	47.1	30.4	23.4	10.8	19.8	29.0	52.9	2.38	
Adapter+AOFT*	79.6	89.6	63.0	84.3	73.7	72.2	22.2	70.7	77.1	86.2	71.2	73.6	77.0	68.2	25.4	39.3	66.8	61.3	42.4	29.9	21.8	44.4	60.9	0.10	
LoRA [10]	75.8	89.9	73.6	99.1	90.8	83.2	57.5	81.4	86.0	95.0	83.4	75.5	85.0	78.1	60.5	46.7	81.6	76.7	51.3	28.0	35.4	57.3	72.0	0.74	
LoRA+AOFT*	78.2	95.0	74.7	99.5	92.0	82.4	59.2	83.3	86.7	95.1	86.0	75.2	85.9	81.5	63.2	50.7	81.0	86.7	53.0	28.8	43.3	60.2	74.3	0.15	

Table 4. This table is extended from ?? in Section 4 and describes the detailed experimental results of the performance comparison on VTAB-1k using ViT-Huge pre-trained on ImageNet-21k as the backbone. Where Full fine-tuning and Linear probing are only used as controls and are not included in the bold comparison. The best results are shown in **bold**.

Methods	Datasets		Natural							Specialized					Structred										Mean Total	Params.(M)
			CIFAR-100	Caltech101	DTD	Flowers102	Pets	SVNH	Sun397	Mean	Camelyon	EuroSAT	Resisc45	Retinopathy	Mean	Clevr-Count	Clevr-Dist	DMLab	KITTI-Dist	dSpr-Loc	dSpr-Ori	sNORB-Azim	sNORB-Ele	Mean		
Full fine-tuning	58.7	86.5	55.0	96.5	79.7	87.5	32.5	70.9	83.1	95.5	81.9	73.8	83.6	47.6	53.9	37.8	69.9	53.8	48.6	30.2	25.8	46.0	63.1	630.90		
Linear probing	64.3	83.6	65.2	96.2	83.5	39.8	43.0	67.9	78.0	90.5	73.9	73.4	79.0	25.6	24.5	34.8	59.0	9.5	15.6	17.4	22.8	26.1	52.7	0.06		
Adapter [9]	69.4	84.4	62.7	97.2	84.2	33.6	45.3	68.1	77.3	86.6	70.8	71.1	76.4	28.6	27.5	29.2	55.2	10.0	15.2	11.9	18.6	24.5	51.5	5.78		
Adapter+AOFT*	67.9	91.3	69.6	98.6	88.1	79.4	49.0	77.7	80.0	95.3	78.3	73.6	81.8	31.5	31.7	39.0	71.6	40.2	22.4	23.8	36.9	37.1	61.5	0.17		
LoRA [10]	63.0	89.4	68.1	98.0	87.0	85.2	48.7	77.1	82.2	94.3	83.1	74.2	83.5	68.6	65.0	44.8	76.4	70.8	48.8	30.4	38.3	55.4	69.3	1.21		
LoRA+AOFT*	68.9	93.0	69.9	98.7	89.1	80.9	51.5	78.8	84.2	94.5	82.1	74.6	83.8	74.1	63.5	46.5	79.3	79.9	48.7	31.5	43.2	58.3	71.3	0.20		

Table 5. This table is extended from Tab. 4 in Section 4 and describes the detailed experimental results of the performance comparison on VTAB-1k using Swin-Base pre-trained on ImageNet-21k as the backbone. The best results are shown in **bold**.

Methods \ Datasets	Natural								Specialized					Structred										Mean Total	Params(M)
	CIFAR-100	Caltech101	DTD	Flowers102	Pets	SVNH	Sun397	Mean	Camelyon	EuroSAT	Resisc45	Retinopathy	Mean	Clevr-Count	Clevr-Dist	DMLab	KITTI-Dist	dSpr-Loc	dSpr-Ori	sNORB-Azim	sNORB-Ele	Mean			
Full fine-tuning	72.2	88.0	71.4	98.3	89.5	89.4	45.1	79.1	86.6	96.9	87.7	73.6	86.2	75.7	59.8	54.6	78.6	79.4	53.6	34.6	40.9	59.7	72.4	86.9	
Linear probing	61.4	90.2	74.8	95.5	90.2	46.9	55.8	73.5	81.5	90.1	82.1	69.4	80.8	39.1	35.9	40.1	65.0	20.3	26.0	14.3	27.6	33.5	58.2	0.05	
MLP-4 [11]	54.9	87.4	71.4	99.5	89.1	39.7	52.5	70.6	80.5	90.9	76.8	74.4	80.7	60.9	38.8	40.2	66.5	9.4	21.1	14.5	28.8	31.2	57.7	4.04	
Partial [11]	60.3	88.9	72.6	98.7	89.3	50.5	51.5	73.1	82.8	91.7	80.1	72.3	81.7	34.3	35.5	43.2	77.1	15.8	26.2	19.1	28.4	35.0	58.9	12.65	
Bias [32]	73.1	86.8	65.7	97.7	87.5	56.4	52.3	74.2	80.4	91.6	76.1	72.5	80.1	47.3	48.5	34.7	66.3	57.6	36.2	17.2	31.6	42.4	62.1	0.25	
VPT-Shallow [11]	78.0	91.3	77.2	99.4	90.4	68.4	54.3	79.9	80.1	93.9	83.0	72.7	82.5	40.8	43.9	34.1	63.2	28.4	44.5	21.5	26.3	37.8	62.9	0.05	
VPT-Deep [11]	79.6	90.8	78.0	99.5	91.4	46.5	51.7	76.8	84.9	96.2	85.0	72.0	84.5	67.6	59.4	50.1	74.1	74.4	50.6	25.7	25.7	53.4	67.7	0.22	
ARC [2]	62.5	90.0	71.9	99.2	87.8	90.7	51.1	79.0	89.1	95.8	84.5	77.0	86.6	75.4	57.4	53.4	83.1	91.7	55.2	31.6	31.8	59.9	72.6	0.27	
RLRR [3]	66.1	90.6	75.5	99.3	92.1	90.9	54.7	81.3	87.1	95.9	87.1	76.5	86.7	66.0	57.8	55.3	84.1	91.1	55.2	28.6	34.0	59.0	73.0	0.41	
LoRA+AOFT*	71.8	92.3	77.1	99.5	92.6	86.4	55.8	82.8	86.9	96.4	87.3	77.6	87.1	84.5	59.3	53.6	84.7	86.8	52.3	28.1	35.5	60.6	73.3	0.14	

$x_i x_j (\cos \varphi - 1)$ can be calculated by this way as follows:

$$\begin{aligned}
x_i x_j (\cos \varphi - 1) &= \frac{q_j}{\sin \varphi} \frac{q_i}{\sin \varphi} (\cos \varphi - 1) \\
&= \frac{q_j q_i}{\sin^2 \varphi} (\cos \varphi - 1) \\
&= -\frac{q_j q_i}{1 + \cos \varphi} = -\frac{q_j q_i}{1 + q_0}.
\end{aligned} \tag{11}$$

Based on Eq. (10) and Eq. (11), we obtain the simplified result as Eq. (5).

E. Detailed Configuration

Tab. 6 summarizes the detailed configurations we used for experiments. As mentioned in Section 4, we utilize grid search to select hyper-parameters such as learning rate, weight decay, batch size, and dropout rate, using the validation set of each task.

F. Experimental details on ablation study

In addition to incorporating our method into the MHA and FFN layers, we also added AOFT solely to the MHA layer. In order to better compare the effects of AOFT in

Table 6. The implementation details of configurations such as optimizer and hyper-parameters. We select the best hyper-parameters for each download task via using grid search.

Optimizer	AdamW
Learning Rate	{0.2, 0.1, 0.05, 0.01, 0.005, 0.001, 0.0001}
Weight Decay	{0.05, 0.01, 0.005, 0.001, 0}
Dropout Rate	{0, 0.1, 0.3, 0.5, 0.7}
Batch Size	{256, 128, 32}
Learning Rate Schedule	Cosine Decay
Training Epochs	100
Warmup Epochs	10

Table 7. Based on the ViT-B backbone, a comparison of the results is presented for applying AOFT to both the FFN and MHA layers, as well as with or without incorporating eigenvalues, on the VTAB dataset.

Methods \ Datasets	Natural								Specialized					Structred										
	CIFAR-100	Caltech101	DTD	Flowers102	Pets	SUNH	Sun397	Mean	Camelyon	EuroSAT	Resisc45	Retinopathy	Mean	Clevr-Count	Clevr-Dist	DMLab	KITTI-Dist	dSpr-Loc	dSpr-Ori	sNOBB-Azim	sNOBB-Ele	Mean	Mean Total	Params.(M)
LoRA($\mathbf{W}_q, \mathbf{W}_v$)	67.1	91.4	69.4	98.9	90.4	85.3	54.0	79.5	84.9	95.3	84.4	73.6	84.6	82.9	69.2	49.8	78.5	75.7	47.1	31.0	44.0	59.8	72.3	0.29
LoRA+AOFT($\mathbf{W}_q, \mathbf{W}_v$)	74.0	91.0	72.7	99.3	89.3	80.6	56.8	80.52	84.9	94.6	82.7	75.6	84.4	71.4	57.5	42.7	82.0	83.4	53.9	22.6	44.5	57.3	71.5	0.08
LoRA+AOFT($\mathbf{W}_q, \mathbf{W}_v, \mathbf{W}_{FC1}, \mathbf{W}_{FC2}$)	75.0	93.2	70.2	99.2	91.1	84.0	57.4	81.7	85.1	95.6	84.7	75.6	85.3	79.8	60.5	49.1	82.0	79.64	54.92	32.7	45.8	60.6	73.4	0.16
Adapter(\mathbf{W}_{FFN})	69.2	90.1	68.0	98.8	89.9	82.8	54.3	79.0	84.0	94.9	81.9	75.5	84.1	80.9	65.3	48.6	78.3	74.8	48.5	29.9	41.6	58.5	71.4	0.16
Adapter+AOFT(\mathbf{W}_{FFN})	74.1	93.9	72.6	99.4	91.0	82.9	57.6	79.0	85.8	95.1	83.4	76.3	84.1	77.7	61.3	49.1	80.0	80.8	53.8	30.4	42.8	58.5	71.4	0.16
Adapter+AOFT($\mathbf{W}_{FFN}, \mathbf{W}_{MHA}$)	67.6	93.9	72.1	99.3	91.6	86.4	53.8	80.7	86.8	95.5	86.0	76.5	86.2	79.0	62.6	51.5	82.7	87.0	54.8	27.7	42.5	60.9	73.5	0.08

the adapter method across different layers, we conducted the following experiments, Tab. 7 shows the experimental results.